

Lift and drag in intruders moving through hydrostatic granular media at high speeds

Fabricio Q. Potiguar*

Universidade Federal do Pará, Departamento de Física, ICEN, Av. Augusto Correa, 1, Guamá 66075-110, Belém, Pará, Brazil

Yang Ding

Aerospace and Mechanical Engineering, University of Southern California, Los Angeles, California 90089, USA

(Received 26 March 2013; published 12 July 2013; corrected 17 July 2013)

Recently, experiments showed that forces on intruders dragged horizontally through dense, hydrostatic granular packings mainly depend on the local surface orientation and can be seen as the sum of the forces exerted on small surface elements. In order to understand such forces more deeply, we perform a two-dimensional soft-sphere molecular dynamics simulation, on a similar setup, of an intruder dragged through a 50–50 bi-disperse granular packing, with diameters 0.30 and 0.34 cm. We measure, for both circular and half-circle shapes, the forces parallel (drag) and perpendicular (lift) to the drag direction as functions of the drag speed, with $V = 10.3$ – 309 cm/s, and intruder depths, with $D = 3.75$ – 37.5 cm. The drag forces on an intruder monotonically increase with V and D , and are larger for the circle. However, the lift force does not depend monotonically on V and D , and this relationship is affected by the shape of the intruder. The vertical force was negative for the half-circle, but for a small range of V and D , we measure positive lift. We find no sign change for the lift on the circle, which is always positive. The explanation for the nonmonotonic dependence is related to the decrease in contacts on the intruder as V increases. This is qualitatively similar to supersonic flow detachment from an obstacle. The detachment picture is supported by simulation measurements of the velocity field around the intruder and force profiles measured on its surface.

DOI: [10.1103/PhysRevE.88.012204](https://doi.org/10.1103/PhysRevE.88.012204)

PACS number(s): 45.70.Mg, 05.10.–a, 64.70.ps

I. INTRODUCTION

Granular matter is a generic name given to a system composed of macroscopic, athermal particles that have mutual repulsive, dissipative interactions [1]. It is an intensely studied field in the physics community given the several distinct behaviors shown by such systems as a consequence of different external conditions imposed on them.

One such condition is that which imposes a flow of particles, named granular flow [2–5]. Within the several granular flow examples, the flow around immersed obstacles has received some attention lately [6–8]. One of the objectives of such investigations is to measure the force in the obstacle due to interactions with the flowing grains, the so-called granular drag [9–14], and lift [14–17].

The drag was studied for several distinct situations: For bodies immersed in slow, dense flows [10,11,14], it was observed that the drag is proportional to the intruder size (cylinder diameter or vane width), to the squared insertion depth, and independent on the mean flow speed; for obstacle within fast, dilute flows [9,12], this force was seen to obey the familiar drag law for flows around spheres in fast viscous flows (proportional to obstacle diameter and to the square of flow speed); finally, studies on impacting bodies [18–20] show that the drag is a sum of gravity, Coulomb friction (depth dependent), and inertial drag (proportional to the square of the penetration speed). This is the granular analog of Poncelet law used in ballistics.

The lift was explored for partially submerged vanes [14,15], where it was seen to scale with several geometrical parameters

of the vane. For horizontally translating objects [16], the lift was seen to depend mainly on the local surface geometry. The lift on a cylinder and a vertical plate was positive, while that on a half-cylinder (with the flat surface facing down) was negative. A calculation based on the forces exerted on small surface elements was able to nicely predict the value observed in the experiments and simulation. Finally, the lift was also investigated in an ellipse immersed in a fast, dilute flow [17] and was seen to vanish for any symmetrical orientation of the obstacle related to the flow direction. In addition, the force calculated for an ideal gas flow of inelastic particles qualitatively reproduced the numerical results, but predicted a smaller force than the one measured in the simulations, since the obstacle is shielded from the incoming flow by the formation of a shock wave.

This work has the main objective of investigating the behavior of the drag and lift forces in a body horizontally translated through a dense granular at constant, high speed. In [16], this force was investigated for a few parameters. Here, we present simulations that extend the parameter ranges used earlier to include values that are not currently accessible to experiments. More specifically, we studied the drag and lift forces on an intruder as a function of the drag speed, the intruder depth and shape. We note that ours is one of the few (if not the only one) studies of forces in intruders in fast, dense conditions.

Our results point to a very interesting behavior of the lift force, which is nonmonotonic dependence on the drag speed and depth. Essentially, we saw that as the drag speed increases, a supersonic granular flow [6–9,11,12,21–23] sets in and, as will be detailed ahead, deeply affects the lift force. Surprisingly, the drag force in this regime (even during the slow transition), increases quadratically with the speed and linearly with depth. This is in contrast to previous supersonic drag

*fqpotiguar@ufpa.br

measurements, in which this force was seen to be independent on the flow speed [11]. On the other hand, it agrees with the results of supersonic dilute flows of [9,12]. Aside from the total force measurements, we also measured flow fields (velocity and number density) as well as force profiles along the intruder surface in order to support our interpretation of the results.

Section II presents the numerical model and parameters used. Section III has all our drag and lift results. These are followed by the fields and profiles data in Sec. IV. Finally, we present our conclusions in Sec. V.

II. SIMULATION DESIGN

The system has $N = 31276$ soft disks (for speed studies) and $N = 46900$ (for depth studies) in a 50–50 bi-disperse mixture with diameters and masses $d_1 = 0.30$ cm, $m_1 = 34.9$ mg and $d_2 = 0.34$ cm, $m_2 = 50.8$ mg. The system is located in a container of length $L_X = 100$ cm.

The force between two contacting disks is given by the model used in [16]. The normal component is

$$\mathbf{F}_{ij}^N = \mathbf{f}_{ij} + \mathbf{f}_{ij}^d. \quad (1)$$

The first term is a conservative part, given by the Hertz law:

$$\mathbf{f}_{ij} = \kappa \delta^{3/2} \hat{\mathbf{r}}_{ij},$$

where $\kappa = 1.04 \times 10^5$ N/m^{3/2} is the hardness, d_i is the i th disk diameter, r_{ij} is the distance between the two disks, $\delta = (d_i + d_j)/2 - r_{ij}$ is the overlap distance, and $\hat{\mathbf{r}}_{ij}$ is a unit vector along the normal between the disks' centers. The second term is a dissipative, velocity dependent force, given by

$$\mathbf{f}_{ij}^d = -\sigma (\hat{\mathbf{r}}_{ij} \cdot \mathbf{v}_{ij}) \delta^{1/2} \hat{\mathbf{r}}_{ij},$$

where $\sigma = 7.28 \times 10^{-2}$ N s/m^{3/2} is the normal damping coefficient and $\mathbf{v}_{ij} = \mathbf{v}_i - \mathbf{v}_j$ is the relative velocity between the disks. The tangential force at the contact point is given by the following expression:

$$\mathbf{F}_{ij}^S = -(\mu_{PP} F_N) \hat{\mathbf{v}}_{ij}^S, \quad (2)$$

where $\mu_{PP} = 0.10$, the static friction coefficient between particles (for particle-intruder contacts, $\mu_{PI} = 0.27$), $F_N = |\mathbf{F}_{ij}^N|$, and $\hat{\mathbf{v}}_{ij}^S$ is the unit vector along the direction of the relative velocity at the contact point. This vector is calculated as

$$\mathbf{v}_{ij}^S = \mathbf{v}_{ij} - (\hat{\mathbf{r}}_{ij} \cdot \mathbf{v}_{ij}) \hat{\mathbf{r}}_{ij} - \left(\frac{d_i \boldsymbol{\omega}_i + d_j \boldsymbol{\omega}_j}{d_i + d_j} \right) \times \mathbf{r}_{ij},$$

where $\boldsymbol{\omega}_i$ is the i th disk angular velocity and $v_{ij}^S = |\mathbf{v}_{ij}^S|$. The total contact force $\mathbf{F}_{ij} = \mathbf{F}_{ij}^N + \mathbf{F}_{ij}^S$ vanishes if the disks are not in contact, i.e., if $\delta < 0$. Finally, each grain suffers the effect of gravity, given by a vertical force,

$$\mathbf{g}_i = -m_i g \mathbf{j}, \quad (3)$$

where $g = 981$ cm/s² is the acceleration of gravity, and \mathbf{j} is a vertical unit vector.

The intruder is either a circle or a half-circle (both with the curved section facing upwards or downwards, which we call inverted half-circle) with a diameter $d_I = 2.54$ cm. It is located, initially, at the position $(x_I = 1.5d_I, y_I = H)$; H is the vertical position of the intruder as measured from the

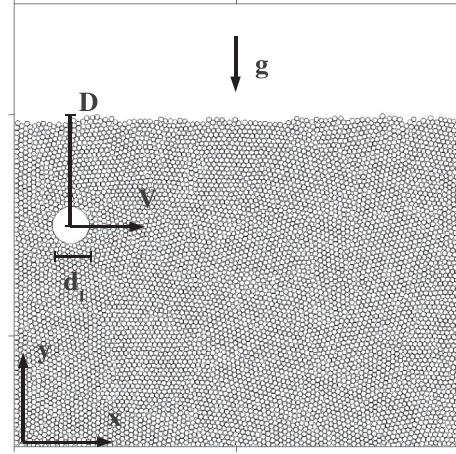


FIG. 1. Pictorial representation of simulation parameters: intruder, of diameter d_I , is dragged at constant depth D , and speed V , under the influence of gravity. The average drag $\langle R \rangle$ is in the $-\mathbf{V}$ direction, while the average lift $\langle L \rangle$ is in either $\pm \mathbf{g}$ direction.

bottom of the container. This parameter is related to the depth D , vertical position measured with respect to the packing free surface, by $D = 30.0 - H$, since for the number of disks and their sizes used here the free surface height, after settling, is ≈ 30.0 cm (for depth studies, the free surface is ≈ 45.0 cm tall); see Fig. 1. The interactions between the disks and the intruders are the same as those given above for two disks.

At the beginning, all disks are randomly generated without overlap among them and with the intruder. At this stage, all intruders are modeled as circles with diameter d_I since this facilitates the overlap check. Then, all disks are allowed to settle under gravity long enough to bring the packing to rest, i.e., when the total kinetic energy per disk is $\approx 10^{-4}$ J.

After the settling phase is finished, the intruder is dragged horizontally, with a constant speed of $V = 10.3\text{--}309$ cm/s, with a total of 16 speeds. We also performed measurements at distinct depths, $D = 3.75\text{--}37.5$ cm, probing 10 distinct depths. Our interest is in the drag R , and lift L forces, respectively, on the intruders as well as flow fields and profiles. The first force is in the negative horizontal direction (opposite to the intruder displacement) while the second is in the vertical direction (perpendicular to the intruder displacement) and can be either positive or negative. All quantities are presented as averages over time and five independent runs. See Fig. 2 for time series examples of such measurements.

Our results can be cast as functions of the Froude number:

$$\text{Fr} = \frac{V^2}{g d_I}.$$

Given our parameters, this number starts at 4.26×10^{-2} and ends at 38.3, spanning four decades in magnitude. As a comparison, the impact experiments of [24] were performed in the range $3.13 < \text{Fr} < 143$. Notice, then, that our speed range, although large, does not include very high Froude numbers. Nevertheless, we will refer later in the text to results at low and high speeds. These adjectives mean that we are considering,

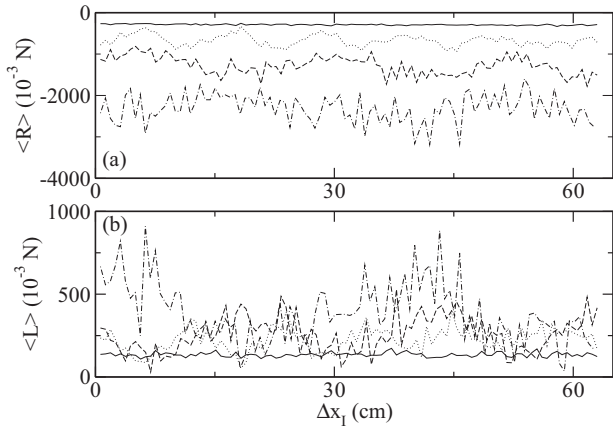


FIG. 2. Drag (a) and lift (b) vs intruder displacement for depth 3.75 cm and speeds (in cm/s): 10.3 (solid), 103 (dotted), 206 (dashed), and 309 (dot-dashed).

respectively, speed values that are in the lower and upper end of our range.

Equations of motion are integrated with a leapfrog scheme [25], with a time step of 0.001. The settling phase is, typically, 10^5 cycles long, while the drag phase is long enough to displace the intruder by $\approx 270d_1$.

III. NUMERICAL RESULTS

The next two subsections have the numerical results for the drag and lift forces on the intruders as functions of the drag speed and depth. In addition, we give a few remarks regarding their interpretation that will be supported with the data for the fields and profiles.

A. Drag force

We begin with the results for the drag as a function of the drag speed, which are shown in Figs. 3 (circle), 4 (half-circle), and 5 (inverted half-circle). We see clearly that the drag monotonically increases with V . In addition, this growth is approximately quadratic: The dashed lines in all three figures are quadratic fits to the $D = 3.75$ cm curves. Fits to the

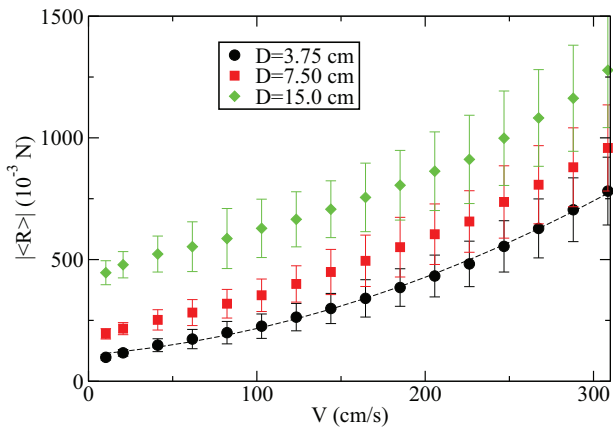


FIG. 3. (Color online) Drag force on the circle as a function of the drag speed and for three distinct depths. Dashed line is a quadratic fit to the $D = 3.75$ -cm data.

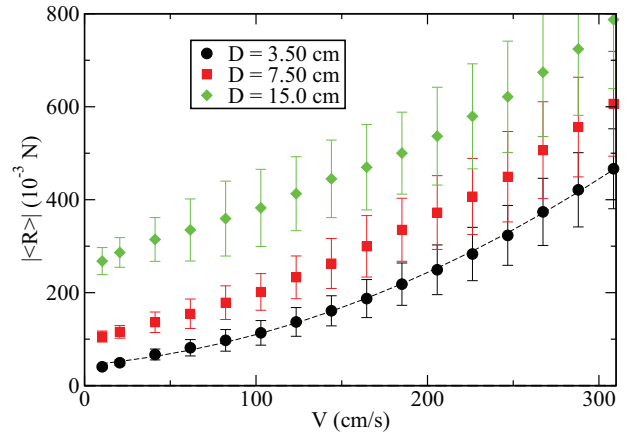


FIG. 4. (Color online) Drag force on the half-circle as a function of the drag speed and for three distinct depths. Dashed line is a quadratic fit to the $D = 3.75$ -cm data.

other curves were made as well and show similar agreement. Therefore, this relationship is barely affected by shape and depth of the intruders. The magnitude of the forces, however, is largest for the circle, while it is approximately equal for both half-circles (with the forces on the inverted one slightly larger). The quadratic dependence on V indicates that the drag follows a similar law to the one of the drag on a sphere dragged through a viscous fluid at a high Reynolds number [9,12,26], i.e., the average net drag comes, mainly, from inertial effects (momentum exchange). In all three figures (Figs. 3–5), the results for $D = 15.0$ cm, especially at low speeds, show evident deviation from the quadratic V dependence. We will show below that the inertial regime is characterized by flow detachment, which means that when the intruder is dragged through the packing, there is a trail of very low density left behind it. Clearly, this trail will appear at a speed that is dependent on the amount of material above the intruder. Therefore, we may understand these deviations as being due to the larger pressure at larger depths which makes the inertial regime set in at higher speeds than those at more shallow depths. More studies are needed to fully characterize the

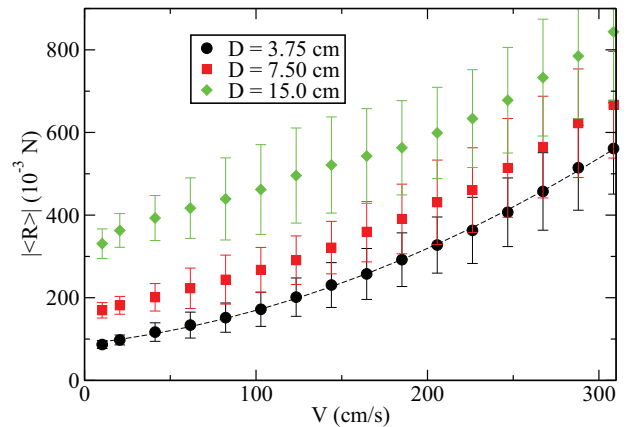


FIG. 5. (Color online) Drag force on the inverted half-circle as a function of the drag speed and for three distinct depths. Dashed line is a quadratic fit to the $D = 3.75$ -cm data.

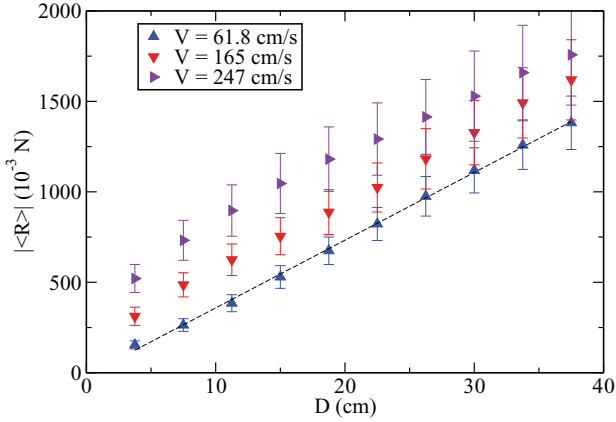


FIG. 6. (Color online) Drag on the circle for varying depths and three distinct drag speed values. Line is a linear fit to the data.

transition to the inertial regime, a task that is postponed to future work.

We saw that the average drag bears a quadratic relationship to the drag speed, and that it is similar to the behavior of the drag force on immersed bodies in fast, viscous flows with the flow speed. The classical fluid dynamics result also linearly relates the drag force to the size of the intruder. To establish that this relationship is the granular analog of the drag law, we should investigate the drag dependence on the intruder size to check for linearity between these two quantities. Preliminary results show that, indeed, the drag is linear in d_I .

The dependence of drag on depth is shown in Figs. 6 (circle) and 7 (both half-circles). Like the results for V , the curves are qualitatively insensitive to shape. We see that the plots follow a linear dependence on D . The three linear fits, one for each shape, confirm this fact. This linear D dependence can be explained by the hydrostatic pressure, typical for our packing conditions. Finally, we see, again, that the drag force for the circle is larger compared to those for both half-circles, which are close to each other. We understand this as a consequence of the circle’s larger projected area perpendicular to the flow, which allows it to push more grains than the other two shapes. We cannot, however, take the net force on the circle as the

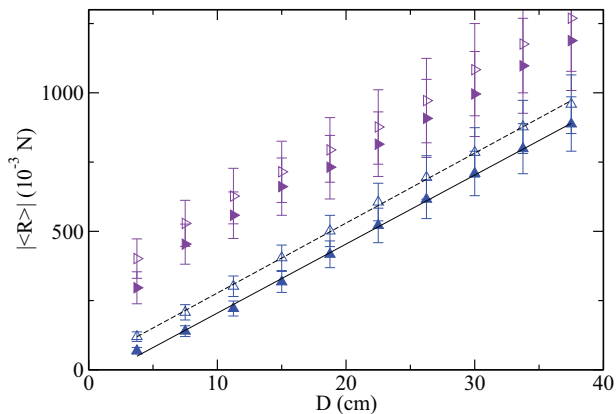


FIG. 7. (Color online) Drag on the half-circle (solid symbols) and inverted half-circle (open symbols) for varying depths and two drag speeds (in cm/s): 61.7 (triangles) and 247 (right triangles). Lines are linear fits to the data.

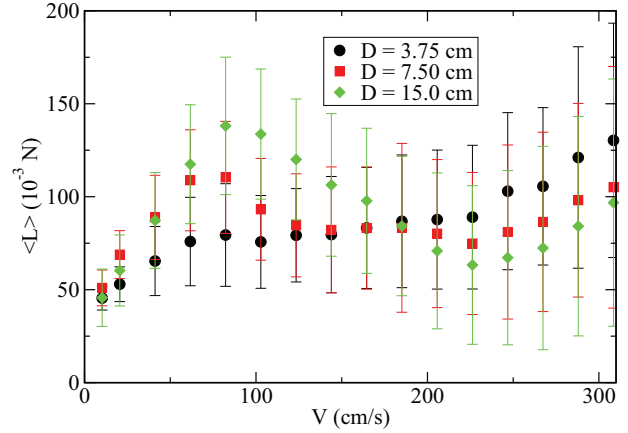


FIG. 8. (Color online) Lift force on the circle as a function of the drag speed and for three distinct depths.

sum of the forces on the half-circles because of large forces at the leading edge of these shapes, a fact seen previously [16] and in our force profiles. We can only make this connection if, when summing up half-circle forces, do not take into account contributions from the flat sides and edges.

B. Lift force

The lift results are shown in Figs. 8 (circle), 9 (half-circle), and 10 (inverted half-circle) as functions of the drag speed.

These plots are in marked contrast to those of the drag forces (Figs. 3–5). As stated in the introduction, the behavior of the lift with drag speed is complex, so let us begin with the circle.

We can see that the curves have three distinct regimes: one at low speeds, in which $\langle L \rangle$ grows with V . The range of this regime seems to be longer for deep intruders: The curve for $D = 15.0$ cm changes behavior at $V = 82.4$ cm/s, while the other two change at $V = 61.8$ cm/s; a second regime at intermediate speeds, where the lift may decrease (deep intruder) or be roughly constant (shallow intruders); and a third regime, appearing at high speeds, $V \geq 227$ cm/s for all depths, shows $\langle L \rangle$ monotonically increasing with V , and this

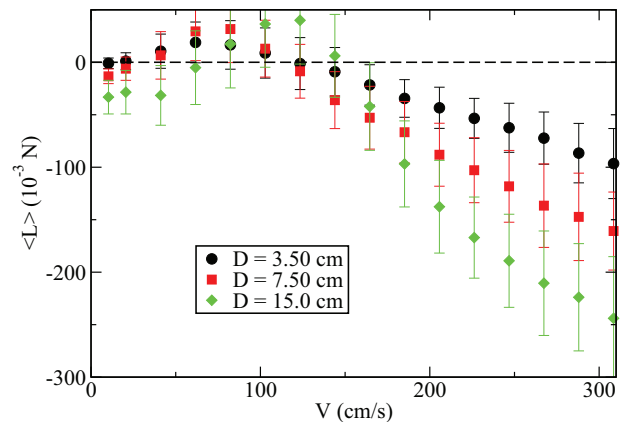


FIG. 9. (Color online) Lift force on the half-circle as a function of the drag speed and for three distinct depths.

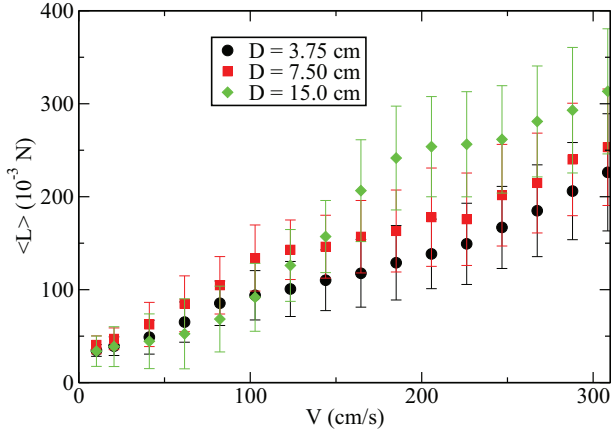


FIG. 10. (Color online) Lift force on the inverted half-circle as a function of the drag speed and for three distinct depths.

growth seems to be linear (we need more data to confirm that this relationship is linear).

For the half-circle, at low drag speed the lift grows with the V , and, interestingly, this growth is such that the lift force inverts its direction at some depth-dependent speed. After $\langle L \rangle$ reaches a maximum (positive) value, it enters the second regime, where it decreases with V and becomes negative again.

For the inverted half-circle (Fig. 10), the lift grows with the drag speed for all depths and speeds. In any case, we still have an initial regime of monotonic growth with V , an intermediate regime (not very clear for the shallowest intruder), and a fast regime, in which the curves are similar to those of the circle.

The dependence of $\langle L \rangle$ on depth for the circle is shown in Fig. 11. We see that, in all three speeds, the lift linearly decreases for high D , as seen from the linear fit to the $V = 247 \text{ cm/s}$ curve. For the slowest intruder, this depth is $D = 15.0 \text{ cm}$ while for the other two, $D = 26.3 \text{ cm}$. The other part of these curves show that, as we increase V , the lift passes from an initial increase, at $V = 61.8 \text{ cm/s}$, to a plateau, at $V = 165 \text{ cm/s}$, to an initial decrease, at $V = 247 \text{ cm/s}$, with D . The last two, however, will eventually grow and reach a maximum before entering the decreasing regime.

The curves for both half-circles, Fig. 12, are markedly different from those of the circle. First, we see that only for the

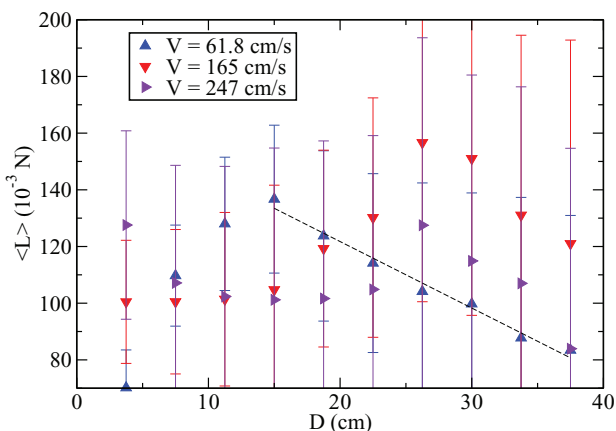


FIG. 11. (Color online) Lift on the circle as a function of intruder depth.

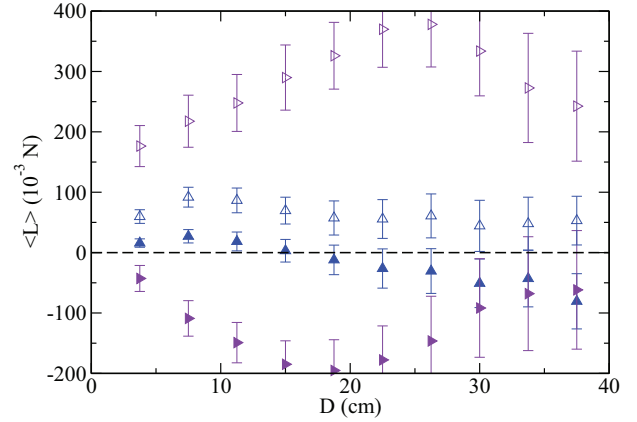


FIG. 12. (Color online) Lift on the half-circle (solid symbols) and inverted half-circle (open symbols) for varying depths and two drag speeds: 61.8 cm/s (triangles) and 247 cm/s (right triangles).

inverted half-circle at high speeds the lift behaves qualitatively similar to the one in the circle. For a fast half-circle, the curve has the inverse relation; it decreases at low depth up to minimum at $D = 18.8 \text{ cm}$, and increases for larger D . For $V = 61.8 \text{ cm/s}$, the lift on the inverted half-circle is not much affected by the depth, except at low D . Finally, we see again the sign inversion phenomenon seen in Fig. 9: The lift is positive, although small, for depths below $D = 15 \text{ cm}$, and negative above this value.

All these results show a very interesting picture: The drag has simple relations with speed and depth, while the lift does not. Both of these forces, however, come from the same kind of interactions, which are grain-intruder repulsive contacts. Therefore, we naturally ask the reasons behind these distinct relations. We know that the forces depend on the number of contacts and the overlap in these contacts (friction is also proportional to the overlap, but is bounded due to Coulomb failure condition, so its influence is limited). These two quantities are not, necessarily, related: A large force could result from a large number of contacts with small overlaps or from a few contacts with strong overlaps. Moreover, a knowledge of both quantities, number of contacts, and contact overlaps does not explain our results. We should also pay attention to the contact position in the intruder surface and to the fact that we measure net forces. The first information is needed because, as shown in [16], the forces depend on the local geometry. The second is important because the drag is the sum of the horizontal forces on the leading and back sides, while the lift is the result of contributions from the vertical forces above and below the horizontal line (the flow direction) that passes through the center of the intruder. Since the results for the net lift have more interesting behaviors, we concentrate our efforts in understanding the reasons that led to the results of Figs. 8–12. Hence, the following analysis deals mainly with data for lift force.

We reasonably assume that the contact overlaps on the leading side increase with V , and those on the back side decrease with speed. In addition, overlaps should increase over the whole intruder for larger depths due to larger packing pressure. Since the drag always increases with V and D , we can easily understand the drag results as the leading drag increasing

faster with increasing speed and depth than that on the back side for the whole range of parameters we studied.

Following this explanation, we conclude that the lift forces above and below the intruder are comparable, since the dependence on V and D is nonmonotonic. The decreasing regimes seen in Figs. 8, 9, 11, and 12 can only occur if the lift on top increases faster with V and D than that on the bottom. In the same way, increasing lift regimes only occur if vertical forces on the bottom grow faster with V and D than those on top. Since the overlaps on the bottom are larger than those on the top, the only way to have decreasing regimes is if some effect occurs with the contact number. Moreover, this effect is not, in principle, the same above and below the intruder. We need to understand the effects of changing speed and depth on the contact number in order to fully understand our results. This is done in the next section where we present data on the lift and contact profiles as well as their contribution from each side of the intruder.

IV. FIELDS AND PROFILES

From the previous discussion, the nonmonotonic relationship between $\langle L \rangle$ and V is the consequence of the unequal, but comparable, forces on the upper and lower sides of an intruder. In addition, these two contributions should have their own relationships with V and D . To have a more clear idea of the effects into play, we show in this section data on the lift and contact profiles along the intruder surface, as well as velocity fields.

Let us begin with the lift profiles $\langle L(\phi) \rangle$. A few examples are shown in Fig. 13 for the circular intruder for $D = 15.0$ cm and eight distinct speed values. We first see that these profiles are consistent with previous numerical results [16], which showed that the force is larger on the lower side than in the upper side (hydrostatic condition) and it is not symmetric with respect to the leading point in the intruder, which allows a vertical plate to have a nonvanishing, positive lift when dragged through the packing.

Another interesting aspect of these profiles is that, as we increase the drag speed, the forces become more concentrated in the range $[-\pi/2, \pi/2]$, with practically zero force outside

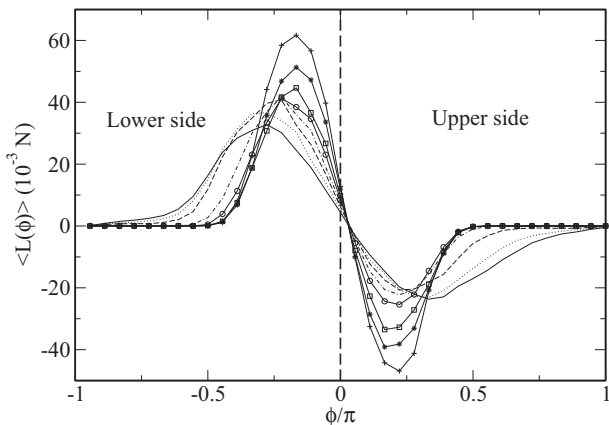


FIG. 13. Lift profiles on the circle for $D = 15.0$ cm. Speeds (in cm/s): 10.2 (solid), 41.2 (dotted), 82.4 (dashed), 124 (dot dashed), 165 (circles), 227 (squares), 268 (stars), and 309 (crosses).

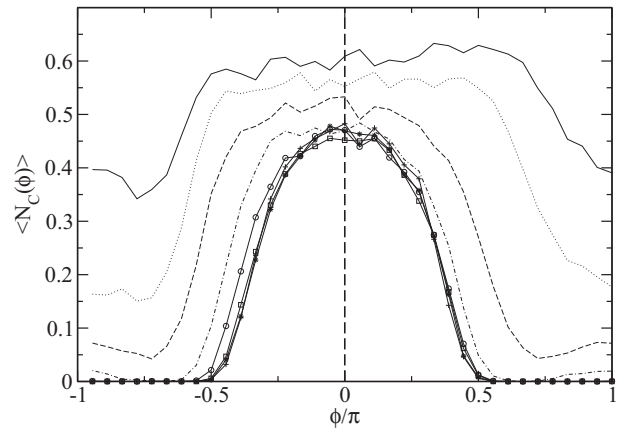


FIG. 14. Contact number profiles for the circle for $D = 15.0$ cm. Speeds (in cm/s): 10.2 (solid), 41.2 (dotted), 82.4 (dashed), 124 (dot dashed), 165 (circles), 227 (squares), 268 (stars), and 309 (crosses).

this range. This feature is also seen in the drag profiles (not shown), $\langle R(\phi) \rangle$, which are symmetrical with respect to $\phi = 0$ and are peaked around this value (the leading end of the intruder). However, in this case, the nonzero elements of the profiles have all the same sign (negative) instead of the positive and negative contributions seen in Fig. 13. This fact naturally leads to a larger net drag compared to a net lift. We conclude, then, that at high speeds, the net drag and lift come from the contribution made only on the leading side of the intruder. At low speeds, the forces are nonzero over the whole surface (a zero force value in the profile means that no grain ever touched the intruder at that point). To confirm this fact, we show in Fig. 14 the contact number profiles for the same cases as those of Fig. 13. Indeed, we see that our previous statement on the concentration of forces on the leading side of the intruder is confirmed. We show, in Figs. 15 and 16, examples of velocity field and packing configuration for high speed. We can see that the zero contact number is a consequence of the appearance of a trail of zero density behind the intruder. Since when it moves it pushes grains up and down, the trail is formed because these thrown grains do not fall back to their initial heights fast enough to fill up the space behind the intruder. It is easy to see that at lower drag speeds, grains will be pushed more gently, up to a point where they merely pass over the intruder

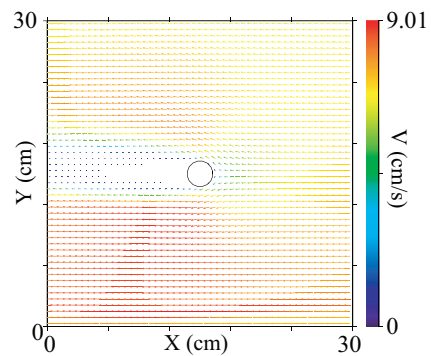


FIG. 15. (Color online) Velocity field, measured in the intruder's frame, in a window 30.0 cm \times 30.0 cm centered on the circle, at $V = 268$ cm/s and $D = 15.0$ cm.

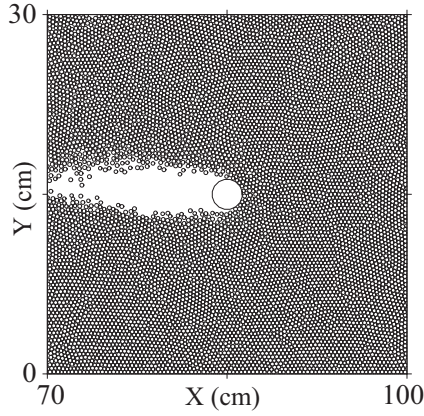


FIG. 16. Local packing configuration around the circle at $V = 247$ cm/s and $D = 15.0$ cm.

(first regime) and the trail is absent. We observed that this effect is depth independent; the trail is always formed for large enough speeds.

The appearance of a vanishing density region behind an intruder is commonplace in studies of supersonic granular flow [6–9,11,12,21–23]. Therefore, we call this effect a granular flow analog of detachment of supersonic fluid flow around obstacles: At high drag speeds, there are only contacts on the leading side of the intruder. The marked distinctions that appear in our results concern the shock front. In the cited reports, shock fronts are seen to be symmetrical regarding the incident flow direction, with a parabolic shape, with a solid region right in front of the leading (stagnation) point in the obstacle. Our shock front is asymmetrical with respect to the drag direction, since gravity is perpendicular to this direction. In addition, we do not observe any parabolic, static configuration in front of the intruder, although there is a typical stagnation point there (see Fig. 15).

From this discussion, it is easy to see that the amount of material above the intruder decreases the height that grains attain when thrown up by the intruder. Therefore, the speed at which the trail appears is affected by depth. We may estimate this speed by calculating the time, t_F , a thrown grain

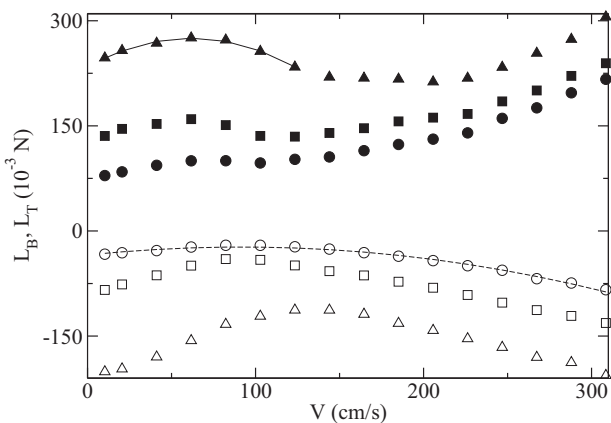


FIG. 17. Lift on top (open) and bottom (solid symbols) of the circle as functions of the drag speed. Depths (in cm): 3.75 (circles), 7.50 (squares), and 15.0 (triangles). Dashed and solid lines are quadratic fits to the data.

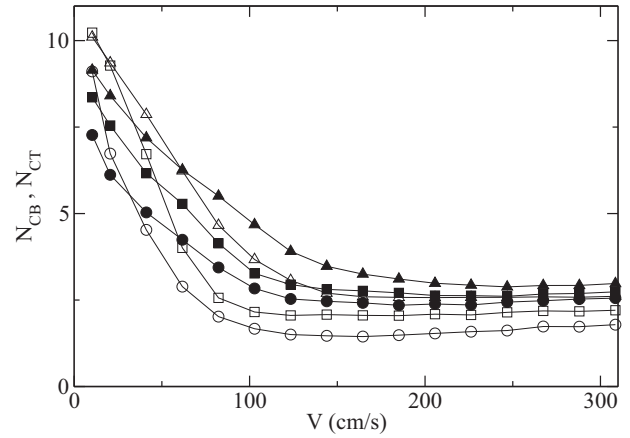


FIG. 18. Contact numbers on top (open) and bottom (solid symbols) of the circle as functions of the drag speed. Depths (in cm): 3.75 (circles), 7.50 (squares), and 15.0 (triangles). Lines are guides to the eyes.

takes to fall a distance h and the time the intruder takes to move an effective radius $(d + d_I)/2$ (assuming that the falling grain and the intruder are at the same horizontal position). A precise estimate can only be given if we can calculate the distance h . Since this is a complicated matter, we need to take into account how the forces are transmitted through the packing and the effects of depth in order to calculate h more accurately; we assume that this height is, simply, one effective radius. Then, the time a grain takes to free fall this distance is

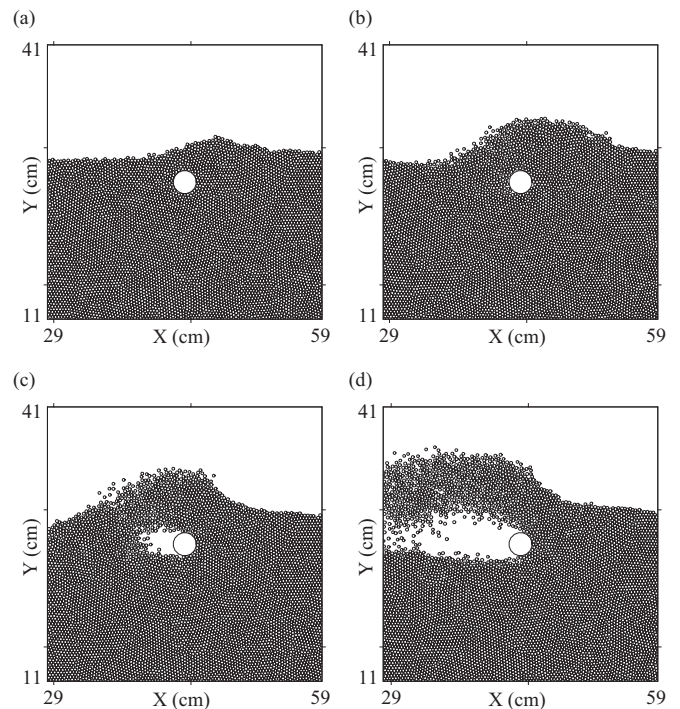


FIG. 19. Configuration snapshots for $D = 3.75$ cm and distinct speeds (in cm/s): (a) 10.3, (b) 61.8, (c) 103, and (d) 165.

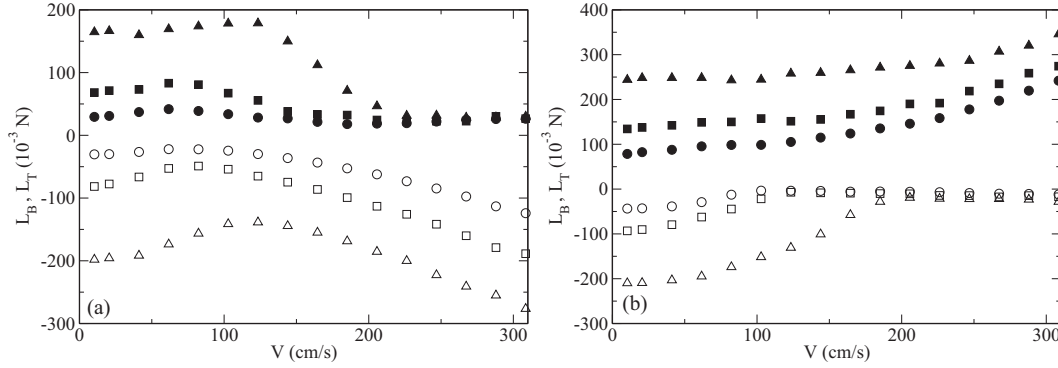


FIG. 20. Lift on top (open) and bottom (solid symbols) of half-circle (a), and inverted one (b), as functions of the drag speed. Depths (in cm): 3.75 (circles), 7.50 (squares), and 15.0 (triangles).

given by

$$t_F = \sqrt{\frac{(d + d_I)}{2g}}$$

The time the intruder moves one effective radius at speed V is

$$t_D = \frac{d + d_I}{2V}$$

The trail occurs when $t_F \geq t_D$. Then, the onset of this phenomenon is given by

$$V = \sqrt{\frac{(d + d_I)g}{2}}$$

From our data, $d = 0.32$ cm (mean particle diameter), $d_I = 2.54$ cm, and $g = 981$ cm/s², the speed value can be calculated to be $V = 37.5$ cm/s. This value is below the speed at which the first regime ends, between 61.7 cm/s and 81.3 cm/s.

In addition, it is clear from Fig. 14 that the overall contact number decreases with V , which confirms our previous argument; the number of contacts is affected by the increase in drag speed. This change, however, does not affect the drag force, since most of its value comes from the leading side. The effect is seen on the lift because the forces on the upper and lower sides of the circle are comparable. We show in Figs. 17 and 18 the values of the lift and contact number on the top and bottom of the circle for all speeds in order to consider each contribution separately.

We see that the top lift has an approximate quadratic dependence on V , like the drag, as suggested by the quadratic fit for the $D = 3.75$ cm curve (dashed line). The bottom lift, on the other hand, shows only one evident quadratic regime at low speeds. This behavior is seen from the quadratic fit to the $D = 15.0$ cm curve. Given the drag results, we feel that the lift on the bottom should be quadratic at all V and that, perhaps due to large noise in lift measurements, also reported in [14], such behavior is hidden in these plots. In any case, we see that the lift behavior at low speeds is correlated to a fast decrease of the contact number on both sides. This fast decrease should be followed by a drop in the forces, which is seen in the top lift. The bottom one, however, increases for low V .

This results can be understood by the following mechanism, illustrated in Fig. 19: When the intruder moves at low speeds [Fig. 19(a)], grains flow upward and increase the free surface height in front of the intruder [16]. This accumulation

will increase the packing pressure and, consequently, the downward vertical force done by the bottom side. As the drag speed is increased [Fig. 19(b)], the bump in the free surface moves from a position in front of the intruder to one right above it. This relieves the packing close to the intruder, and the bottom lift decreases. As the speed is increased even further, [Figs. 19(c) and 19(d)], the material is thrown up in the air and the trail behind the intruder is formed. At high speeds, the contact number reaches a plateau, which means that all forces depend on V mainly through increasing pressure on the leading side.

The conclusions we reached for both sides of the circle also hold for the half-circles. Comparing Figs. 9 and 10 with those for the top and bottom lift, respectively, we see that they are qualitatively similar. It implies that the contacts on the flat side should not have a severe change with V , even though they are the reason the lift inverts the sign for the half-circle. The lift and contacts on the flat side show a distinct picture. Our results (Fig. 20) reveal that the lift force on the flat sides, on both half-circle shapes, decrease as we increase the speed and reach practically the same value at high V , independent on depth, although the initial values of this force grow with D . This high speed plateau is an obvious consequence of flow detachment. When the flow begins to detach from the intruder,

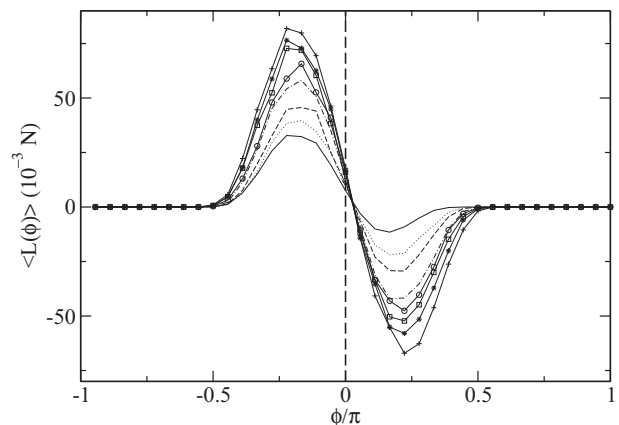


FIG. 21. Lift profiles on the circle for $V = 247$ cm/s. Depths (in cm): 3.75 (solid), 7.50 (dotted), 11.25 (dashed), 18.75 (dot dashed), 22.00 (circles), 25.75 (squares), 29.50 (stars), and 33.25 (crosses).

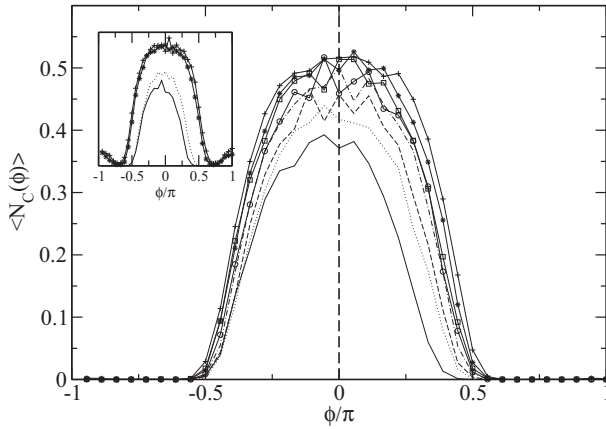


FIG. 22. Contact number profiles for the circle at $V = 247$ cm/s. Depths (in cm): 3.75 (solid), 7.50 (dotted), 11.25 (dashed), 18.75 (dot dashed), 22.00 (circles), 25.75 (squares), 29.50 (stars), and 33.25 (crosses). (Inset) $V = 168$ cm/s; depths follow the same convention as main graph.

practically all contacts on the flat side will disappear, since there is no projected area perpendicular to the flow. Forces will only be exerted on the leading point, which barely changes with V and D when the flow detaches. Finally, this independence of the lift on V and D explains why the lift on the half-circle only decreases after it reaches its maximum, positive value.

Let us look at the lift and contact profiles as functions of depth in Figs. 21 and 22. The main feature of these plots is the overall increase of both quantities with depth and the familiar flow detachment, consistent with hydrostatic conditions. Our results also show that flow detachment can be suppressed at a given depth for a suitable speed. This is clear from the inset of Fig. 22, which shows contact profiles for intermediate speed. At low depths, contacts occur only on the leading side, $\phi = [-\pi/2, \pi/2]$. For deep intruders, we find a nonzero contact number all over the intruder surface. Our results suggest we should go to a shallower position, at lower speeds, in order to see flow detachment.

In Figs. 23 and 24, we show the lift and contact numbers on the top and bottom sides of the circle as a function of depth. It is clear that the bottom lift is linear in D for all speeds, and

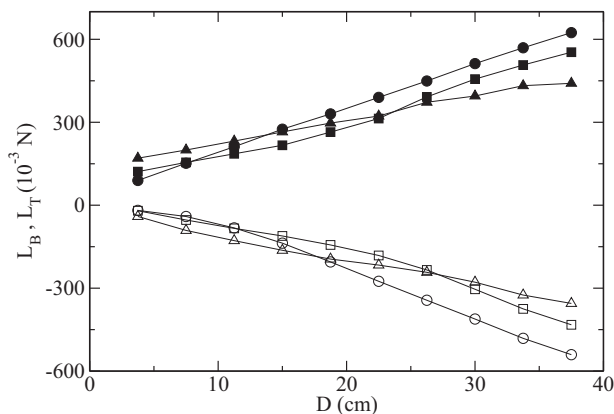


FIG. 23. Lift on top (open) and bottom (solid symbols) of the circle as functions of depth. Speeds (in cm/s): 61.8 (circles), 165 (squares), and 247 (triangles). Lines are guides to the eyes.

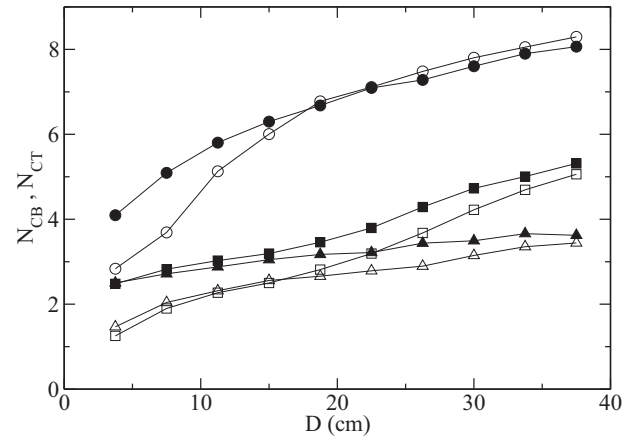


FIG. 24. Contact numbers on top (open) and bottom (solid symbols) of the circle as functions of depth. Speeds (in cm/s): 61.8 (circles), 165 (squares), and 247 (triangles). Lines are guides to the eyes.

it changes slower with depth for high drag speeds. The top lift curves, however, do not suggest unique linear dependence between lift and depth, except for the $V = 247$ cm/s curve. The other two show two distinct linear regimes, one at low and the other at high speeds. Looking at the contact numbers, we see that the contact numbers have two distinct regimes with depth: a fast growth one at low D , and a slower variation one at higher depths. These results might explain the reason that the top lift changes behavior at some depth. This is consistent with previous speed results that showed that when the drag speed is below $V = 227$ cm/s, the lift value is affected by changes in the contact numbers. It also explains why the initial fast growth of the top contact number with depth does not affect the lift value.

For the half-circles, we show in Fig. 25 the top and bottom lifts as functions of depth. We see, again, the familiar depth independence of the lift on the flat side. In this case, it appears at high speed and low depth. Again, we can understand this result in view of the fact that flow detachment can be suppressed for suitable speed and depth. At low depth and high speeds, flow detaches. As the depth is increased, this phenomenon is decreased, and the net lift linearly increases with D , as seen in Fig. 12. For other cases, the lift force increases approximately linear on depth.

V. CONCLUSIONS

We presented numerical results of the forces, drag, and lift, on an intruder dragged horizontally through a hydrostatic granular packing, as functions of the drag speed V , depth D , and shape. We saw that the net drag increases quadratically with V and linearly with D , and is larger for the circular intruder. The net lift, however, depends nonmonotonically on both V and D and is lower for the circle. We found that the sign of the net lift force depends on V and D , as seen on the results for the half-circle. For the other two shapes, the net lift was always positive.

This complex behavior can be explained by detachment of the flow, i.e., decrease in the overall grain-intruder contact

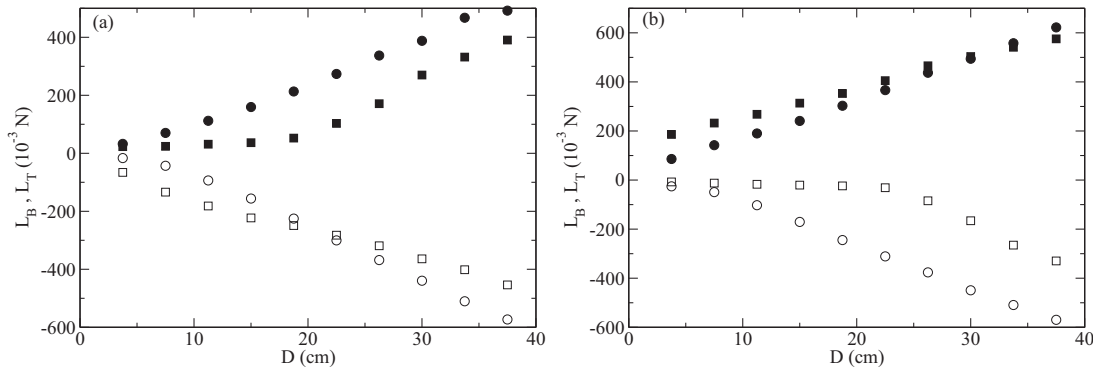


FIG. 25. Lift on top (open) and bottom (solid symbols) of half-circle (a), and inverted one (b), as functions of depth. Speeds (in cm/s): 61.8 (circles) and 247 (squares).

number. This effect decreases the forces on the intruder. Since this decrease is not the same on the upper and lower parts of the intruders with V , in some speed range the lift force on the lower side grows faster than the one on the upper side, which increases the net lift. The other effect is also seen; the lift on the upper part grows faster than the lift on the lower part, which is consistent with a decrease of the net lift. The effect of this phenomenon on the flat side of the half-circles is that all forces on this side are done on the leading point, since the flow is deviated at this point and barely touches the flat side at high V . Finally, we see that this effect can be suppressed by a high depth.

We also showed that the vertical forces on the top and bottom sides of the intruders follow similar relationships with V and D as those for the net drag $\langle R \rangle$. This is to be expected, since all forces are contact grain-intruder interactions.

Future possibilities of these studies are on a detailed description of the forces within the packing as the intruder is dragged. If we know how the intruder will affect the forces in the flow, we will be able to predict much more accurately the beginning of flow detachment and why it does not occur in the same on both sides of an intruder. In addition, a more detailed description of the lift on both top and bottom sides

may lead to an empirical force law similar to those of the drag force obtained in [9,12].

Finally, other shapes might show interesting results as well. For instance, we observed that if we drag an ellipse, we can also see a sign inversion for the lift as we saw in the half-circle case. In addition, this sign inversion seems to be dependent only on the angle of attack of the ellipse. Obviously, this effect depends also on eccentricity, speed, and depth. If we understand this effect, we might be able to design more efficiently robots that move in granular environments, as those proposed in [27], as well as understand better how animals locomote in sand [28].

ACKNOWLEDGMENTS

We are in debt with Daniel I. Goldman for his time in discussing and questioning from the point where the simulations were set up until the manuscript was finished. This work is financially supported by Coordenação de Aperfeiçoamento de Pessoal de Nível Superior (CAPES), Conselho Nacional de Desenvolvimento Científico e Tecnológico (CNPq), and Fundação Amazônia Paraense (FAPESPA) (Brazilian agencies).

-
- [1] H. M. Jaeger, S. R. Nagel, and R. P. Behringer, *Rev. Mod. Phys.* **68**, 1259 (1996).
 - [2] K. Wieghardt, *Annu. Rev. Fluid Mech.* **7**, 89 (1975).
 - [3] C. S. Campbell, *Annu. Rev. Fluid Mech.* **22**, 57 (1990).
 - [4] I. Goldhirsch, *Annu. Rev. Fluid Mech.* **35**, 267 (2003).
 - [5] GDR Midi, *Eur. Phys. J. E* **14**, 341 (2004).
 - [6] Y. Amarouchene, J. F. Boudet, and H. Kellay, *Phys. Rev. Lett.* **86**, 4286 (2001).
 - [7] E. C. Rericha, C. Bizon, M. D. Shattuck, and H. L. Swinney, *Phys. Rev. Lett.* **88**, 014302 (2001).
 - [8] J. F. Boudet, Y. Amarouchene, and H. Kellay, *Phys. Rev. Lett.* **101**, 254503 (2008).
 - [9] V. Buchholtz and T. Poeschel, *Granular Matter* **1**, 33 (1998).
 - [10] R. Albert, M. A. Pfeifer, A.-L. Barabasi, and P. Schiffer, *Phys. Rev. Lett.* **82**, 205 (1999).
 - [11] D. Chehata, R. Zenit, and C. R. Wassgren, *Phys. Fluids* **15**, 1622 (2003).
 - [12] C. R. Wassgren, J. A. Cordova, R. Zenit, and A. Karion, *Phys. Fluids* **15**, 3318 (2003).
 - [13] M. P. Ciamarra, A. H. Lara, A. T. Lee, D. I. Goldman, I. Vishik, and H. L. Swinney, *Phys. Rev. Lett.* **92**, 194301 (2004).
 - [14] R. Soller and S. A. Koehler, *Phys. Rev. E* **74**, 021305 (2006).
 - [15] K. Wieghardt, *Mech. Res. Comm.* **1**, 3 (1974).
 - [16] Y. Ding, N. Gravish, and D. I. Goldman, *Phys. Rev. Lett.* **106**, 028001 (2011).
 - [17] F. Q. Potiguar, *Phys. Rev. E* **84**, 061302 (2011).
 - [18] L. S. Tsimring and D. Volfson, in *Powders & Grains*, edited by R. Garcia-Rojo, H. Hermann, and S. McNamara (Bokuna, Leiden, 2005).
 - [19] H. Katsuragi and D. J. Durian, *Nat. Phys.* **3**, 420 (2007).
 - [20] D. I. Goldman and P. Umbanhowar, *Phys. Rev. E* **77**, 021308 (2008).

- [21] Y. Amarouchene and H. Kellay, *Phys. Fluids* **18**, 031707 (2006).
- [22] J. F. Boudet, J. Cassagne, and H. Kellay, *Phys. Rev. Lett.* **103**, 224501 (2009).
- [23] J. F. Boudet and H. Kellay, *Phys. Rev. Lett.* **105**, 104501 (2010).
- [24] A. M. Walsh, K. E. Holloway, P. Habdas, and J. R. de Bruyn, *Phys. Rev. Lett.* **91**, 104301 (2003).
- [25] D. C. Rapaport, *The Art of Molecular Dynamics Simulation*, 2nd ed. (Cambridge University Press, Cambridge, 2007).
- [26] L. D. Landau and E. M. Lifshitz, *Fluid Mechanics*, 2nd ed. (Elsevier, Oxford, 2007).
- [27] R. D. Maladen, Y. Ding, P. B. Umbanhowar, and D. I. Goldman, *Int. J. Rob. Res.* **30**, 793 (2011).
- [28] R. D. Maladen, Y. Ding, C. Li, and D. I. Goldman, *Science* **325**, 314 (2009).